Article

Photophysical Behavior of mNeonGreen, an Evolutionarily Distant Green Fluorescent Protein

Frederik Steiert,[1,2] Eugene P. Petrov,[1,3] Peter Schultz,[1] Petra Schwille,[1] and Thomas Weidemann[1,*]

[1]Department of Cellular and Molecular Biophysics, Max Planck Institute of Biochemistry, Martinsried, Germany; [2]Physics Department, Technical University Munich, Garching, Germany; and [3]Faculty of Physics, Ludwig Maximilian University of Munich, Munich, Germany

ABSTRACT   Fluorescent proteins (FPs) feature complex photophysical behavior that must be considered when studying the dynamics of fusion proteins in model systems and live cells. In this work, we characterize mNeonGreen (mNG), a recently introduced FP from the bilaterian *Branchiostoma lanceolatum*, in comparison to the well-known hydrozoan variants enhanced green fluorescent protein (EGFP) and *Aequorea coerulescens* GFP by steady-state spectroscopy and fluorescence correlation spectroscopy in solutions of different pH. Blind spectral unmixing of sets of absorption spectra reveals three interconverting electronic states of mNG: a nonfluorescent protonated state, a bright state showing bell-shaped pH dependence, and a similarly bright state dominating at high pH. The gradual population of the acidic form by external protonation is reflected by increased flickering at low pH in fluorescence correlation spectroscopy measurements, albeit with much slower flicker rates and lower amplitudes as compared to *Aequorea* GFPs. In addition, increased flickering of mNG indicates a second deprotonation step above pH 10 leading to a slight decrease in fluorescence. Thus, mNG is distinguished from *Aequorea* GFPs by a two-step protonation response with opposite effects that reflects a chemically distinct chromophore environment. Despite the more complex pH dependence, mNG represents a superior FP under a broad range of conditions.

INTRODUCTION

Labeling by fluorescent proteins (FPs) undoubtedly transformed cell biology (1–3) and concomitantly catalyzed a wide spectrum of microscopic technologies providing unprecedented spatial and temporal resolution (4,5). The prospects of *Aequorea victoria* green fluorescent proteins (avGFPs) were soon recognized and led to enormous activity for improving and diversifying the FP toolkit for multicolor imaging and a vast number of advanced biophysical applications (6–8). To image at reduced autofluorescence in tissue or cells, research efforts focused in particular on the search for red-shifted variants, whose properties with respect to higher-order oligomer formation, brightness, and photostability were steadily improved (9,10). Considering FPs now cover the entire visible spectrum, it appears quite remarkable that in the green color range, some classic avGFPs, like enhanced green fluorescent protein (EGFP), remained largely unrivalled.

Recently, this situation was challenged by the introduction of the novel FP mNeonGreen (mNG) (11), which was engineered based on a yellowish precursor isolated from the phylogenetically distant cephalochordate *Branchiostoma lanceolatum* (12). Numerous mutations were identified to eliminate the tendency to form tetramers and, in turn, to maintain high levels of fluorescence (11). As a result, mNG features single maxima in excitation and emission spectra ($\lambda_{ex,max}$ = 506 nm, $\lambda_{em,max}$ = 517 nm), which are slightly red-shifted as compared to EGFP ($\lambda_{ex,max}$ = 488 nm, $\lambda_{em,max}$ = 507 nm). Because mNG is characterized by a much higher molar absorptivity (116,000 M^{-1} cm^{-1}) and fluorescence quantum yield (0.8), its brightness exceeds that of EGFP by ~50% when using 488-nm laser light excitation with the same power density and the commonly used 505-nm long-pass emission filter for GFPs. Further, it was convincingly demonstrated that mNG performs well as a universal genetic fusion tag when testing for subcellular distributions of various fusion constructs by confocal fluorescence imaging (11). Up to now, mNG has been used in a couple of genetic studies (13,14) including the development of a calcium sensor (15). However, the photophysics of mNG has not yet been addressed in greater depth.

One way to characterize structural features of FPs is to study spectral perturbations in buffers of different composition. Although the compact structure of the β-barrels

provides remarkable stability and shielding from the bulk solvent (16), a number of buffer components can affect fluorescence (17). For example, fluorescence quenching of the wild-type avGFP in acidic buffers is reproducible to an extent that it served as a signature to assess correct refolding of the protein (18). The dual absorption bands (∼400 nm, short wavelength, A-band; ∼475 nm, long wavelength, B-band) were assigned early on to the protonated-neutral and deprotonated-anionic chromophore states, respectively (17). This picture received strong support by the concept of excited state proton transfer (ESPT), a mechanism by which deprotonation of the chromophore precedes fluorescence emission. ESPT explains why in wild-type avGFP, absorbance through the A-band results in emission spectra that resemble the B-band (but not exactly, and therefore termed intermediate state I) (19,20). The hydrogen-bonding networks in avGFPs that enable ESPT are well understood (21–23). Protonation of the chromophore takes place at the hydroxy group of the tyrosine side chain Y66 (amino acids in one letter code) that points toward a gap in the β-sheets of the barrel surface (24). The local strand separation surrounding H148, located opposite to the chromophore, represents a well-studied gateway for proton and water exchange between the chromophore-bearing compartment and bulk solution (25–27). The abundance of A- and B-band contributions in absorption spectra was henceforth taken as a proxy for the protonation state of the chromophore. Subsequently, substituted side chains in the immediate chromophore environment were studied in numerous avGFP mutants by steady-state spectroscopy at different pH levels (23,28–33). However, whether this wealth of information is sufficient for the understanding of evolutionarily more distant bilaterian FPs remains an open question.

The recently solved crystal structure of mNG appears to represent a conventional 11-stranded barrel-shaped FP (34). The chemical structure of the chromophores of EGFP and mNG is identical; key residues for the cyclization reaction like E222 and R96 (avGFP numbering; in mNG E220, R98 (11)) occur in mNG at the conserved positions. The chromophore is formed by the tripeptide sequence GYG, similar to *A. victoria* yellow fluorescent proteins (avYFPs). However, unlike class 4 avYFPs (3), mNG does not contain coplanar aromatic groups in the vicinity of the chromophore (34), and thus π-stacking (24) is ruled out in mNG. At neutral pH, mNG features a single B-band (11), suggesting that the chromophore exists mainly in the anionic form, which would associate mNG with class 2 avGFPs such as EGFP (3). The presence of the GYG-chromophore and the absence of π-stacking might explain the rather moderate red shift of the mNG emission relative to EGFP as compared to classical avYFPs showing a more red-shifted spectrum (35). Considering the many replacements at the primary sequence level (less than 30% sequence similarity relative to EGFP), we were interested in which ways the photophysical properties of mNG differ from those of *Aequorea* GFPs and whether unique features can be identified for this evolutionarily distant FP family.

To study photophysics, it is beneficial to combine bulk solution measurements with single-molecule techniques. In particular, molecular brightness depends on the dynamics of short-lived dark states. In solution, individual FPs rapidly sample various conformational substates, and therefore fluorescence emission shows considerable heterogeneity. Accordingly, the photon stream of single FPs exhibits complicated patterns covering a broad range of timescales: blinking phenomena lasting from subseconds to minutes, as they were first detected in time-lapse single-molecule imaging (36) (not addressed in this work), and fluorescence flickering at timescales of microseconds to milliseconds, as it was discovered by fluorescence correlation spectroscopy (FCS) (37). Flickering reflects rapid interconversions between chromophore states of sufficiently different quantum yield, mostly treated as bright and fully dark states (38). The response to protonation of many avGFPs variants is surprisingly uniform, showing a significant rise of the flicker fractions in FCS autocorrelation functions (ACFs) that corresponds well with the acid-quenching behavior of bulk solutions (37,39–43). However, single-molecule fluorescence fluctuation data bear no inherent structure to decide on the type of chemical reaction. For example, transition rates between anionic-bright and protonated-dark chromophore states of EGFP were evaluated with different sets of rate equations and slightly different molecular models (37,42,43). Because the evaluation of kinetic constants requires a priori knowledge about the chromophore structure, the combination of FCS with steady-state spectroscopy is fruitful: both approaches operate under equilibrium conditions, and FPs can be measured in the very same buffers. However, due to the different concentration regimes and excitation power densities at which these methods work, consistency between steady-state spectroscopy and FCS is not always easy to achieve.

Here, we study the protonation response and the photophysical behavior of purified bilaterian mNG in comparison to hydrozoan variants EGFP and *Aequorea coerulescens* green fluorescent protein (AcGFP) in buffers covering a wide range of pH values. With our aim to bridge the single-molecule regime with ensemble measurements, we consistently combine steady-state absorption and fluorescence spectroscopy with confocal FCS. In particular, a quantitative analysis of absorption spectra by blind spectral unmixing distinguishes three protonation-dependent electronic states in mNG: a bright state dominating between pH 6–10 and two additional states building up in the acidic and basic regimes. Correspondingly, we detect two major transitions in the FCS data: a very moderate flickering in the acidic regime and an unexpected rise of the flicker fractions in the basic regime. The results are discussed in light of the recently published crystal structure and emphasize some structural differences between hydrozoan and bilaterian FPs.

MATERIALS AND METHODS

Cloning and purification of FPs

Coding sequences for EGFP (pEGFP-N1; Clontech, Takara, Saint-Germain-en-Laye, France), AcGFP1 (pLVX-AcGFP1-N1; Clontech), and mNG (pmNeonGreen-N1; Allele Biotechnology, San Diego, CA) were amplified, digested with BamHI/NotI, and ligated into pET-28a(+) vectors to obtain a sequence coding for the FP, a linker sequence (AAALE, amino acids in one letter code), and a C-terminal hexahistidine stretch (His-tag; H6). Using pET-28a(+) as a template, the His-tagged FPs were amplified again, digested with BamHI/MfeI, and ligated into pEGFP-N1 to obtain the final FP expression vectors: pEGFP-H6-N1, pAcGFP-H6-N1, and pmNG-H6-N1. For bacterial expression, we used the plasmid pNCSmNeonGreen (Allele Biotechnology). Additional information about primers, plasmids, and protein purification can be found in the Supporting Material.

Absorption spectroscopy

Absorption spectra were measured with a 10-mm light path in 100-μL quartz cuvettes (105.201 QS; Hellma, Müllheim, Germany) with a VP-450 photometer (JASCO, Groß-Umstadt, Germany) at a scan speed of 400 nm/min. Absorption spectra of mNG in buffer were measured within the spectral interval of 250–600 nm with a step of 1 nm and spectral slit width of 1 nm. Solutions of mNG and EGFP with different pH were prepared by adding trace amounts of HCl or NaOH. Absorption spectra were measured after 2 min equilibration time within the spectral interval of 250–600 nm with 1 nm steps and spectral slit width of 1 nm. To account for pipetting inaccuracies, spectra were normalized to the absorbance at 278 nm.

To analyze the absorption data, we represented the set of spectra recorded at m wavelengths for n different pH values as an $m \times n$ matrix $\mathbf{A}$. The number of independent components contributing to the set of spectra represented by matrix $\mathbf{A}$ corresponds to its practical numerical rank k, which can be determined (44) using singular value decomposition. Once the number k of independent spectral components is estimated, one can carry out blind spectral unmixing to estimate the spectral features of the individual components as well as their contributions to the total spectrum depending on the control parameter (pH in this study). To do that, we employed a numerical technique of approximate nonnegative matrix factorization (NNMF) (45). This approach allows one, for a given nonnegative $m \times n$ matrix $\mathbf{A}$ and an integer $k < \min\{m,n\}$, to find nonnegative matrices $\mathbf{W}$ and $\mathbf{H}$ of dimensions $m \times k$ and $k \times n$, respectively, such that their product $\mathbf{WH}$ approximates $\mathbf{A}$ as close as possible, in the sense of minimizing the sum of squared residuals $SSR = \|\mathbf{A} - \mathbf{WH}\|_F^2$. From the viewpoint of an analysis of a set of measured absorption spectra represented by matrix $\mathbf{A}$, the NNMF technique allows one to obtain estimates of spectral features of individual k components, which, in this notation, constitute columns of matrix $\mathbf{W}$, and the contributions of the respective components to the total spectrum as a function of pH, which are represented by lines of matrix $\mathbf{H}$. Robust algorithms for numerical solution of this problem have been described previously (45) and are relatively easy to implement.

In our implementation, we used a combination of the multiplicative update (MU) (46) and alternating least-squares algorithms (47). For the initial search, we employed the MU algorithm, which, if initialized with strictly positive matrices $\mathbf{W}$ and $\mathbf{H}$, preserves their positivity throughout iterations. We initialized the columns of $\mathbf{W}$ with the mean values of the corresponding columns of $\mathbf{A}$, whereas random numbers uniformly distributed on the interval (0, 1) were used to initialize entries of matrix $\mathbf{H}$. A Monte Carlo search of the optimum solution was performed by repeatedly running the MU algorithm 1000 times with random initializations of $\mathbf{H}$ and selecting the output {$\mathbf{W},\mathbf{H}$} that provides the smallest SSR. The results are further refined by the alternating least-squares algorithm, which was initialized using the matrices $\mathbf{W}$ and $\mathbf{H}$ produced at the previous stage.

To guarantee nonnegativity of $\mathbf{W}$ and $\mathbf{H}$ in this step, the nonnegative least squares procedure is employed (48). Finally, to ensure that the sums of contributions of the components for all values of the control parameter (pH) are close to unity in the least-squares sense, the results were rescaled as follows: $\mathbf{W}_{out} = \mathbf{WR}^{-1}$ and $\mathbf{H}_{out} = \mathbf{RH}$. Here $\mathbf{R} = \text{diag}(\mathbf{r})$, and vector $\mathbf{r}$ is a least-squares solution of the system of equations $\mathbf{H}^T\mathbf{r} = \mathbf{e}$, where $\mathbf{e}$ is a column n-vector with all entries equal to 1. The whole procedure was repeated 100 times, the resulting component spectra and their contributions as a function of pH were averaged, and the corresponding mean-square errors were calculated.

Steady-state fluorescence spectroscopy

Fluorescence excitation and emission spectra were measured in 100-μL quartz cuvettes with a JASCO FP-8500 fluorescence spectrometer (JASCO, Easton, MD), using a spectral slit width of 2.5 nm in both the excitation and emission channels and a scan speed of 500 nm/min. Protein stock solutions in phosphate buffer (50 mM sodium phosphate, 100 mM NaCl, pH 7.5) were diluted to ~350 nM into the same buffer. Solutions with different pH were prepared by adding trace amounts of HCl or NaOH and equilibrating the sample for 2 min before measurement. Fluorescence excitation and emission spectra were normalized to the absorbance at 278 nm. Total fluorescence intensities were calculated from emission spectra by integrating the signals in the range of 505–650 nm.

FCS

With confocal FCS, temporal signal fluctuations are measured in a microscopic focal volume that is statically placed in a solution of fluorescent molecules. Fluctuating fluorescence signals are recorded and correlated in time, and the resulting correlation functions are analyzed by models that describe chromophore transitions to transient dark states as well as diffusion through a three-dimensional Gaussian-shaped detection volume (5,38).

FCS was performed with a confocal laser-scanning microscope LSM780 (Carl Zeiss AG, Jena, Germany) equipped with the Confocor3 extension. The temperature of the sample was 28 $\pm$ 1°C. The GFP excitation/detection settings included the argon laser line with a wavelength of 488 nm, the corresponding dichroic mirror, a water immersion objective (C-Apochromat 40$\times$/NA1.2 W Korr UV-Vis-IR, Carl Zeiss AG), the confocal pinhole (34 μm = 1 Airy unit), and a long-pass filter (LP 505 nm). To suppress detector-dependent artifacts (afterpulsing), autocorrelation was recorded in the cross-correlation mode using a 50/50 beam splitter and two independent detectors, which allowed us to reliably measure short flickering in the lower microsecond range (49). The excitation power density defined as $I = 2P/(\pi w_0^2)$ could be varied in the range of 0.1–800 kW/cm^2; routine FCS measurements were performed at 0.6 kW/cm^2. Here, P is the total power of the exciting laser beam that was determined using a microscope-slide power meter (S170C; Thorlabs, Munich, Germany) at the objective lens. The parameter w_0 is the 1/e^2 radius of the confocal detection volume in the focal plane, which was determined in calibration measurements based on the diffusion time $\tau_D = w_0^2/(4D)$ of Alexa Fluor 488 (Thermo Fisher Scientific, Waltham, MA) in water at 28 $\pm$ 1°C and using its reported diffusion coefficient of $D = 414 \pm 10$ μm^2/s at 25°C (50) adjusted to 28°C. To better resolve transient dark states related to FP chromophore flickering from diffusion-related fluorescence intensity fluctuations (51), we expanded the confocal detection volume by varying the pupil filling (ZEN software; Carl Zeiss AG) at the back aperture of the objective. Measurements were carried out with 15% ($w_0 = 0.96 \pm 0.04$ μm), 20% ($w_0 = 0.74 \pm 0.01$ μm), or 100% pupil filling ($w_0 = 0.20 \pm 0.01$ μm) as indicated.

For FCS measurements, protein stock solutions stored in phosphate-buffered saline (pH 7.5) were diluted to 5 nM in 10 mM potassium phosphate buffer, for which the pH was adjusted by trace amounts of HCl or NaOH. Samples were equilibrated for at least 15 min at room

temperature in #1.5 borosilicate glass-bottom slides (eight-well, Lab-Tek; Thermo Fisher Scientific) before mounting. Fluorescence intensity time traces were recorded and correlated in real time by the proprietary ZEN software (Carl Zeiss AG). For each condition, the results of 30-s-long measurements were averaged over 30 runs. ACFs were analyzed with *PyCorrFit* (v0.9.8) software by applying the T-T-3D model function (52)

$$G(\tau) = G^T(\tau)G^D(\tau), \qquad (1)$$

containing two exponential prefactors to account for fluorescence intensity flickering because of transient dark states

$$G^T(\tau) = \left(1 + \frac{T_1}{1 - T_1}e^{-\frac{\tau}{\tau_1}}\right)\left(1 + \frac{T_2}{1 - T_2}e^{-\frac{\tau}{\tau_2}}\right), \qquad (2)$$

as well as a factor describing diffusion-driven number fluctuations in a Gaussian-shaped detection volume

$$G^D(\tau) = \frac{1}{N}\left(1 + \frac{\tau}{\tau_D}\right)^{-1}\left(1 + \frac{\tau}{SP^2\tau_D}\right)^{-\frac{1}{2}}. \qquad (3)$$

For fitting, τ_1 and τ_2 were constrained to the ranges of 1–5 μs (very fast flickering or triplet transitions) and 10–1000 μs (flickering), respectively. The structure parameter $SP = 5$ was kept fixed at a typical instrumental value obtained from Alexa Fluor 488 measurements in buffer. Amplitudes for flickering (T_1 and T_2) were kept free. For FCS measurements at varying pH, we used low excitation intensities (0.6 kW/cm^2). For fitting pH-dependent FCS data of mNG, we assigned an additional slow τ_3 (>1000 μs) for external protonation-dependent flickering while keeping the diffusion time fixed to an average value that was determined under neutral-to-basic conditions.

All FCS measurements were corrected for noncorrelated background intensity B contributing to the signal $S = F + B$ in the respective channels (indexed 1 and 2):

$$\frac{1}{N} = G^D(0) = G^D_{\text{exp}}(0)\left(\frac{F_1}{F_1 - B_1}\right)\left(\frac{F_2}{F_2 - B_2}\right). \qquad (4)$$

The molecular brightness was expressed by counts per particle: $CPP = F/N$.

RESULTS

Absorbance at different pH

To investigate the electronic substates of purified mNG (for details, see the Supporting Material), we measured steady-state absorption spectra in buffers of different pH. The buffer system was first validated by EGFP, for which we observed the well-documented B-to-A-band conversion upon acidification, featuring an isosbestic point at 427 nm and a pK_a = 5.9 $\pm$ 0.1 (Fig. S1) in good agreement with the published results (37). At neutral pH, the absorption spectrum of mNG is dominated by the long-wavelength B-band with a maximum at 506 nm (11). Reminiscent of avGFPs, when acidifying the buffer, mNG builds up a short-wavelength A-band with a maximum at ~400 nm, whereas the magnitude of the B-band decreases. The transition features an isosbestic point at 440 nm observed

exclusively in the acidic regime (Fig. 1 *A*); in acidic buffers, the position of the B-band maximum is maintained within ± 1 nm. In contrast to EGFP, mNG shows a distinct behavior under basic conditions, in which the absorption maximum shows a gradual blue shift from 505 nm at pH 8.0 to 499 nm at pH 10.8 (Fig. 1 *B*). A small decrease of the peak absorbance is accompanied by a build-up of a shoulder at ~475 nm. This, along with an additional iso-sbestic point at 493 nm observed exclusively in the basic regime, suggests that the distinct changes in the basic regime are due to interconversion of two forms with different but closely overlapping spectra. Altogether, the observed behavior indicates the existence of at least three spectroscopically distinct forms of mNG.

With the intention of identifying elementary components in our set of spectra, we carefully defined the pH range at which each of the isosbestic points were maintained. Absorption spectra of mNG in solutions below pH 3.8 showed a global gradual blue shift of ~10 nm between pH 3.8 and 3.2, leaving a broad A-band-shaped absorption peak centered at 390 nm (Fig. S2 *A*). Because the magnitude of the blue shift matches the one that is observed for wild-type avGFP after acid denaturing (53), at pH 3.2, the integrity of the mNG β-barrel might already be lost. Importantly, below pH 3.8, the spectra do not cross the isosbestic point at 440 nm anymore, whereas the residual shoulder located at the position of the B-band is still present. Thus, pure
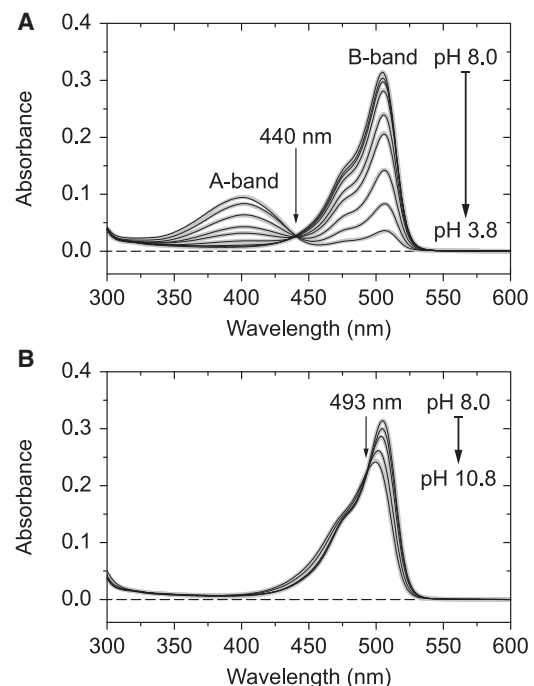

FIGURE 1 Absorption spectroscopy of mNG in 10 mM potassium phosphate of varying pH. (*A*) Absorption spectra in the acidic and (*B*) the basic regime are shown. Black hairlines represent experimental spectra; thick gray lines represent spectra recovered based on the results of blind spectral unmixing (Fig. 2). The isosbestic points are indicated by arrows.

A-band absorption is not accessible within the system of states characterized by the isosbestic point at 440 nm. Similarly, in the basic regime beyond pH 10.8, the spectra become unstable and show a slow but pronounced kinetics (Fig. S2 B) transforming the most basic shape of the spectrum into a broader, strongly blue-shifted feature while maintaining yet another isosbestic point at 457 nm. Again, the blue shift of ∼20 nm is reminiscent of what was observed for base-denatured wild-type avGFP (53), suggesting a partial denaturing of mNG at pH 11.3. The transformation progresses with a rate constant of $0.026 \pm 0.003 \ \mathrm{min}^{-1}$ and approaches a mixed state featuring two peaks (Fig. S2, B–D). Taken together, we found that both isosbesic points (440 and 493 nm) that govern the behavior at moderate pH values are maintained in the pH range of 3.8–10.8.

Within this pH range, the analysis of the singular values of the matrix composed of the experimentally measured absorption spectra revealed that three independent spectral components are necessary to represent the set of absorption spectra for the given level of experimental errors. We were able to obtain their spectral features (Fig. 2 A) and contributions (Fig. 2 B) using blind spectral unmixing based on NNMF (for details, see Materials and Methods). The results reveal that the contributions of all three components show a pronounced pH dependence: the mNG absorption spectra around the neutral pH are dominated by the component
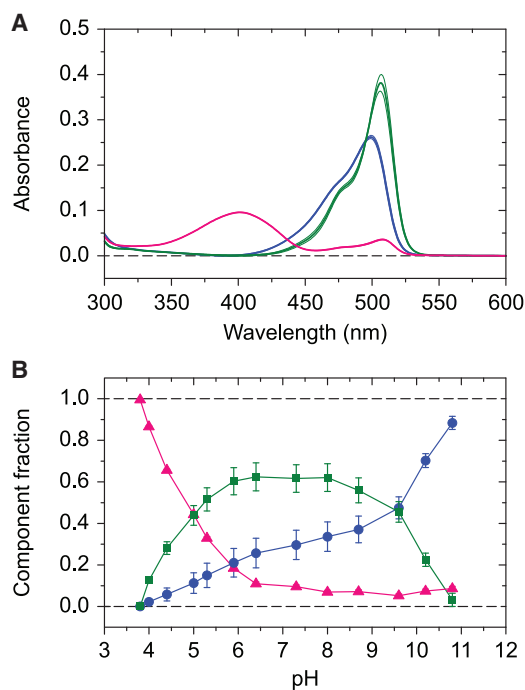

FIGURE 2 Blind spectral unmixing of mNG absorption spectra in the pH range 3.8–10.8. (A) Reconstructed spectra of the coexisting chromophore states dominating the acidic (*magenta*), the neutral (*green*), and the basic (*blue*) pH range (hairlines represent one standard deviation error bounds) and (B) their relative contributions at varying pH (same color code as in (A)) are shown.

with a maximum of 506 nm ("neutral form") showing a bell-shaped pH dependence, reaching ∼60% at the neutral pH and vanishing in the acidic and basic regimes. The second component showing strong A-band absorption corresponds to the protonated state of mNG ("acidic form"). Although the component dominates in the acidic environment with a fraction of more than 80% at pH 4.0, its contribution rapidly vanishes at and above the neutral pH. A third component, featuring a maximum at 495 nm and a pronounced shoulder at 450 nm, dominates in the basic regime ("basic form"), its contribution reaching ∼90% at pH 10.8. Interestingly, below pH 10, the basic form vanishes rather slowly, following an almost linear pH dependence. As a consequence, at physiological pH, ∼30% of mNG is still in the basic form, whereas between pH 5 and 6 all three forms coexist, with significant contributions exceeding 10%.

We noticed that the reconstructed spectrum of the acidic form of mNG shows an unexpected shoulder at 508 nm, a position characteristic of the B-band. Therefore, the question arises whether the spectrum of the acidic form correctly reflects the properties of the acidic form or rather contains an artifactual ghost band resulting from the restricted pH range used in spectral unmixing. Revisiting the EGFP absorption spectra showing a single isosbestic point as a control, we observed a similar phenomenon: blind spectral unmixing returns the spectra close to the outmost pH extremes as elementary forms, whereby the acidic form still shows a nonvanishing shoulder at the position of the B-band (Fig. S3 A). Of note, the resulting $pK_a = 6.01 \pm 0.03$ calculated from the contributions was slightly higher (Fig. S3 B) compared to the published value based on bulk fluorescence (37) and our own data (Fig. S1 B). The small shift may indicate a small but significant overestimation of the abundance of the acidic form, probably owing to the long-wavelength shoulder.

To further systematically address this point for mNG, in which three chromophore states are involved, we performed blind spectral unmixing for the same data set with different boundaries of the pH range (Fig. S4). In the acidic regime, the shoulder at 508 nm indeed progressively decreases as the lower pH boundary gradually approaches pH 3.8 from above, whereas the spectral shapes of the neutral and basic forms remain stable (Fig. S4 A). Concomitantly, the contribution of the acidic form is reduced at the benefit of the neutral form, whereas the contribution of the basic form remains largely unaffected (Fig. S4 B). Likewise, when the upper pH boundary gradually approaches pH 10.8 from below, an increasingly blue-shifted spectrum of the basic form is recovered, whereas the spectral shapes of the neutral and acidic forms remain stable (Fig. S4 C), and the basic form reduces its contribution at the benefit of the neutral form (Fig. S4, C and D). We believe that such trends could be used to identify and remove ghost bands and extract pure spectral shapes that better reflect the physical properties of

the chromophore; this intriguing question, however, lies outside the scope of the current work. For our mNG and EGFP examples, we can state that the errors related to the ghost bands are expected to remain below 10%.

Steady-state fluorescence at different pH

Fluorescence excitation and emission spectra of mNG measured as a function of pH show the behavior that qualitatively follows that of absorption (Fig. 3 A). In the acidic regime, the spectral shapes and the maxima are maintained for both excitation and emission ($\lambda_{ex,max}$ = 506 nm; $\lambda_{em,max}$ = 517 nm), whereas for the basic regime, a gradual hypsochromic shift is observed (~7 nm for excitation spectra and ~4 nm for emission spectra). Normalizing to the protein content at 278 nm indicates that the emission maxima decrease under acidic and basic conditions, when fluorescence is excited at the absorption B-band. With λ_{ex} = 400 nm, the fluorescence emission ($\lambda_{em,max}$ = 517 nm) is reduced to less than 1% compared to the emission excited at λ_{ex} = 488 nm. In contrast to 488-nm excitation, the emission maxima observed with λ_{ex} = 400 nm

grow with increasing pH (data not shown). Because the A-band-excited fluorescence intensity would decrease with increasing pH, we associate this fluorescence with the minor emission of the basic form because of its low absorption at 400 nm (see Fig. 2 A). As such, either the plateau of residual contributions of the acidic form in the basic regime is insignificant (Fig. 2 B), or ESPT is negligible in mNG.

The pH-dependent total fluorescence intensity of mNG (λ_{ex} = 488 nm) is highest at neutral pH and decreases toward both acidic and basic conditions, showing a more dramatic drop in the acidic regime (Fig. 3 B). Because we had determined the relative fractions of three potential chromophore states by absorption spectroscopy, the total intensity can be interpreted as a sum of their individual contributions weighted by a product of the corresponding absorbance at a given excitation wavelength and the respective fluorescence quantum yields. Assuming that each of these forms has a pH-independent quantum yield, the problem of how these forms contribute to the total fluorescence intensity therefore constitutes a system of three linear equations, for which the quantum yield of two forms can be calculated relative to a third. Considering the acidic form to be nonfluorescent and taking the neutral form as a reference, we determined the relative quantum yield of 0.90 ± 0.04 for the basic form (Fig. 3 B). Notably, the fit shows a slight systematic deviation below pH 5, which we attribute to the residual long-wavelegth shoulder (ghost band—for details, see Discussion) of the acidic form that induces small errors in the contributions of all forms. Despite this uncertainty, the plateau of total fluorescence intensity of mNG within the pH range of 7–10 is fairly well-reconstructed by the co-existing neutral and basic forms, showing approximately the same molecular brightness for excitation at 488 nm.
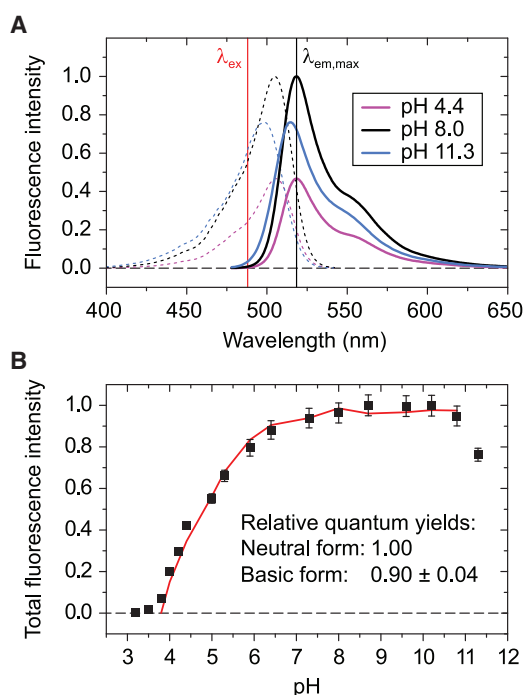
FCS under neutral conditions

To characterize freely diffusing mNG in comparison to EGFP and AcGFP (for protein sequences, see Supporting Material) in greater detail, we applied FCS, a single-molecule-sensitive method to analyze fluorescent molecules in a small detection volume in free solution (5,38). To better resolve transient dark states related to chromophore flickering from purely diffusion-related fluorescence intensity fluctuations, we expanded the focal volume by varying the degree of back aperture underfilling. Larger focal volumes shift the corresponding ACFs to longer lag times, reflecting the prolonged dwell times, whereas rates of photophysical processes remain unaffected. At moderate excitation powers, representative ACFs for mNG in phosphate buffer at pH 8.0 show the characteristic decay that is dominated by the dwell time of the molecules in the detection volume (Fig. S5 A). Under neutral conditions, for all three FPs, the measured ACFs could satisfactorily be fitted with a model containing up to two prefactors describing flickering (triplet transitions or photoinduced isomerization/protonation), as

FIGURE 3 Steady-state fluorescence of mNG. (*A*) Excitation and emission spectra measured in acidic (*magenta*), neutral (*black*), and basic (*blue*) phosphate buffer are shown. Although neutral and acidic emission maxima superimpose (*black vertical line*), the basic spectra are blue shifted. A typical GFP excitation wavelength is shown for comparison (488 nm, *red vertical line*). (*B*) The pH-dependence of total fluorescence intensity (emission range 505–650 nm) of mNG (*black squares*) is shown. The pH range subjected to blind spectral unmixing (pH 3.8–10.8, Fig. 2 B) was used to reconstruct the total fluorescence intensity (*red line*) based on the relative contributions of the basic and neutral form; for details, see text.

well as a single-component expression for diffusion-related fluorescence fluctuations. The latter assumes a three-dimensional Gaussian shape of the detection volume, which is justified by the very good fit for different degrees of underfilling. Irrespectively of the size of the detection volume, the diffusion coefficients (mNG: $97 \pm 9 \ \mu m^2/s$; EGFP: $99 \pm 9 \ \mu m^2/s$; AcGFP: $99 \pm 12 \ \mu m^2/s$) of all three FPs were in good agreement to literature (54) and testify to the absence of any FP aggregates after purification (Fig. S5 *B*).

Additionally, we addressed the excitation power density as an important experimental starting point for the FCS analysis. We consistently used a detection spot size with $w_0 = 0.74 \ \mu m$ as a compromise, providing a significantly larger focal volume at high enough excitation power densities (0.1–2 kW/cm^2). Under neutral buffer conditions, the ACF of all three FPs contains flickering at two different timescales. One is a very fast flicker process in the range of 1–5 μs, contributing only little to the overall amplitude, that is independent of both pH and excitation power and, thus, unlikely to be associated with triplet transitions (51). We determined the highest contribution of very fast flickering for EGFP (2.1 μs; 13%) followed by AcGFP (2.4 μs; 5%) and mNG (2.4 μs; 4%) (data not shown). In contrast, a distinct excitation-power dependence was observed for another flicker process at timescales of several hundred

microseconds, showing a consistent increase in rate and amplitude for all three FPs (Fig. S6, *A–C*), suggesting that this transition is photoinduced. The associated correlation times are longest for AcGFP (up to 600 μs) and shortest for mNG (up to 400 μs), with photoinduced flicker amplitudes smallest for EGFP, followed by mNG ($\sim$40% higher than EGFP) and AcGFP ($\sim$80% higher than EGFP).

FCS at different pH

We next performed FCS measurements in phosphate buffer solutions that were used for bulk spectroscopy and covering the same range of pH. Because sample preparations inevitably vary in concentration when diluting to the nanomolar regime, parameters linked to absolute number of particles show scatter that markedly exceeds the error in FCS measurements. We therefore focused on the molecular brightness (counts per particle, CPP) as a readout that does not depend on the exact concentration. FCS measurements of EGFP at different pH illustrate a typical FP response to protonation. Consistent with the view that chromophore protonation affects fluorescence emission, fast photoinduced flickering on the timescale of several hundred microseconds increases dramatically at low pH. For EGFP under acidic conditions, both exponential decays are clearly visible in
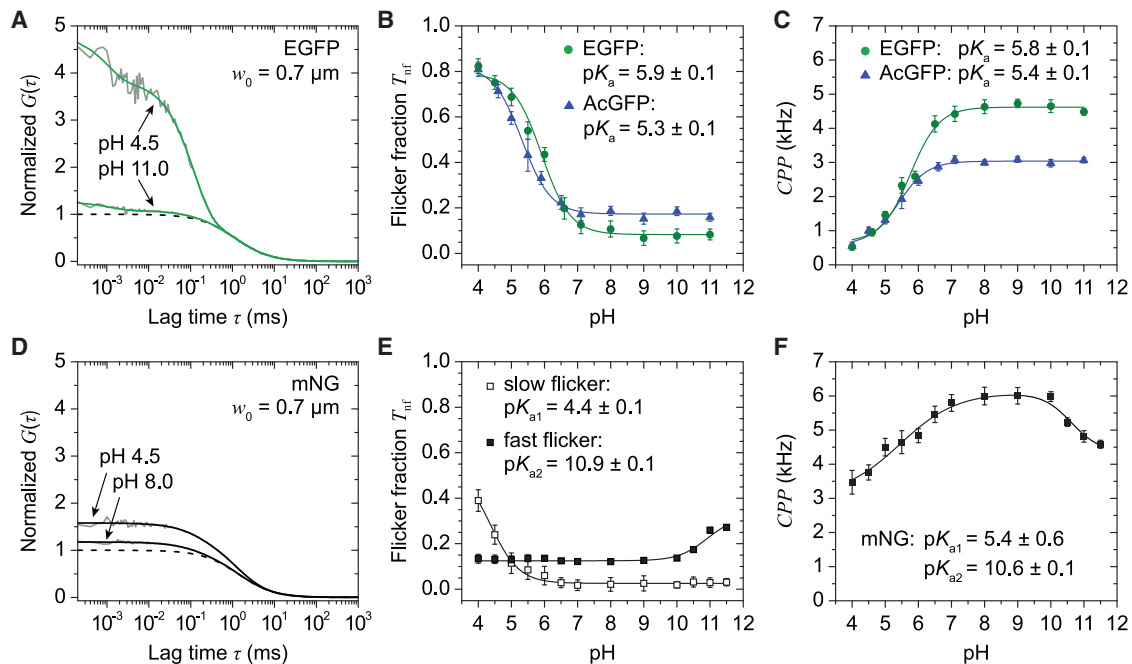

FIGURE 4 FCS measurements of EGFP, AcGFP and mNG at varying pH. (*A*) ACFs of EGFP illustrating the effect of protonation are shown. Note the pronounced increase of the amplitudes due to very fast flickering and photoinduced flickering with respect to diffusion-related contributions (*dashed line*). (*B*) The pH-dependence of the fast photoinduced flicker fractions of EGFP and AcGFP is shown. (*C*) The CPPs of EGFP and AcGFP decrease in the acidic regime, reflecting the increasing fraction of FPs lingering in transient dark states. (*D*) ACFs of mNG illustrating the effect of protonation show rather slow flickering of moderate amplitude (diffusion-related contributions, *dashed line*). (*E*) The pH-dependence of fast photoinduced flicker fractions (*open squares*) and slow flicker fractions (*filled squares*) of mNG is shown. Note the additional flickering that builds up at high pH. (*F*) The CPP of mNG decreases at both ends of the pH spectrum. Below pH 9, the molecular brightness of mNG is consistently increased with respect to *Aequorea* GFPs (*C*). The fitting of sigmoidal inflections with an expression for dose-response curves returned pK_a values for each transition. To see this figure in color, go online.

the ACF and can be well-separated from diffusion (Fig. 4 A). The magnitude of the pH-dependent response is quite similar for EGFP and AcGFP, as reflected by the concurrent rise of the fast flicker fraction below pH 6 (Fig. 4 B). The flickering-related amplitude (flicker fraction) increases from a constant plateau of ~8% (EGFP) and 17% (AcGFP) under neutral and basic conditions to more than 80% under acidic conditions for both FPs. The behavior of flicker fractions is paralleled by the flicker rates, showing a stable plateau between pH 7 and 11 followed by a systematic increase below pH 6 (Fig. S7 A). The plateau was previously interpreted as an internal protonation-dissociation reaction involving the chromophore and a closely located proton acceptor site (37). Fitting of sigmoidal dose-response curves yielded $pK_a = 5.9 \pm 0.1$ for EGFP in very good agreement with spectroscopic data (37) and $pK_a = 5.3 \pm 0.1$ for AcGFP, for which, to our knowledge, no reference value is available. Correspondingly, EGFP and AcGFP show a progressive decrease of CPP in the acidic regime characterized by about the same pK_a values (Fig. 4 C).

The picture for mNG is, however, more complicated. Compared to *Aequorea* GFPs, the visible protonation-driven increase of the flicker amplitudes under acidic conditions is moderate (Fig. 4 D). When keeping all correlation times free during fitting, the amplitudes of photoinduced flickering (several 100 μs) seemed to decrease at lower pH. The corresponding CPP therefore stayed apparently constant over the entire acidic range (data not shown). The fit result was clearly in contradiction to the ensemble measurements, in which we see a distinct fluorescence quenching at low pH (Fig. 3 B). Revisiting the fit parameters, we noticed that the diffusion times of mNG decreased at low pH, indicating that an additional process interfering at this timescale was left unaccounted for. Reevaluating the ACFs with a fixed diffusion time typical for the neutral-to-basic conditions revealed an additional slow flicker process at timescales of several milliseconds, reminiscent of what Widengren et al. observed for EGFP using larger detection volumes (51). Each of the amplitudes associated with fast (~150 μs) and slow flickering (~2.5 ms) showed distinct changes at either extreme of the pH spectrum: the fractions of photoinduced flickering remain constant at a level of 13 $\pm$ 1% over a broad pH range and increase only above pH 9, whereas slow flickering is undetectable in the neutral and basic regime and exclusively builds up below pH 7 (Fig. 4 E). Thus, the slow flickering of mNG can be associated with external protonation of its chromophore.

Interestingly, all three flicker rates of mNG show remarkable stability across the entire pH range (Fig. S7 B). Taking both fast and slow flickering into account, the CPP progression (Fig. 4 F) qualitatively resembles the bell-shaped total fluorescence intensity as it was observed in ensemble measurements (Fig. 3 B), supporting the above assumption of pH-independent quantum yields of the distinct neutral and basic chromohore forms.

FCS using diffraction limited settings

Finally, to compare the molecular brightness (CPP) of mNG with the two *Aequorea* GFPs across a broader excitation power range, we returned to diffraction-limited illumination (Fig. 5). Although too-low excitation powers suffer from insufficient statistics, too-high excitation powers can also pose problems, because additional photophysical processes like triplet transitions, photobleaching, and fluorescence saturation may lead to considerable distortion of the ACFs. Therefore, one is usually interested to operate in a regime in which the fluorescence intensity scales linearly with the excitation power.

Under neutral conditions, in which the acidic form of mNG is absent, two flicker times were sufficient to fit the data of all three FPs. Although all parameters were kept free during the fit, the prior knowledge from experiments with enlarged focal volumes turned out to be crucial for fitting at the limit of low excitation intensities, at which diffusion- and flickering-related fluctuations are indistinguishable. At intensities larger than 10 kW/cm², diffusion times are strongly affected by photobleaching and saturation, whereas additional excitation-driven triplet transitions build up at very short correlation times of several microseconds (data not shown). At higher powers of ~100 kW/cm², the molecular brightness values reach a maximum to finally decrease and converge to approximately the same value. The decrease at extremely high laser powers has been previously explained by photobleaching via higher-order excited states (55). As a result, the CPP determined for all three FPs at nanomolar concentrations is a remarkably stable parameter: at low powers, mNG shows consistently a threefold higher molecular brightness compared to AcGFP and a 1.4-fold higher molecular brightness relative to EGFP.

To determine the power density range at which the fluorescence is proportional to excitation, we quantified the downward deviation from the linear dependence of CPP
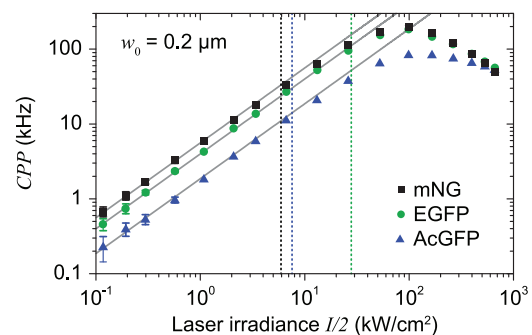

FIGURE 5 Molecular brightness of mNG (*black squares*), EGFP (*green circles*), and AcGFP (*blue triangles*) determined across a broad excitation power density range with a diffraction limited focal volume. At lower excitation powers, the CPPs increase linearly (*gray lines*, slope 1) with the excitation power density. Excitation powers at which the CPP deviated down from the linear dependence by 10% (*colored vertical lines*) were used to determine the saturation intensity (I_s); for details, see text.

values due to fluorescence saturation as compared to the linear increase represented by low excitation powers (Fig. 5). A 10% loss is reached at 5.9 kW/cm^2 for mNG (corresponding saturation intensity $I_s = 53$ kW/cm^2), at 7.6 kW/cm^2 for AcGFP ($I_s = 68$ kW/cm^2), and at 27.9 kW/cm^2 for EGFP ($I_s = 251$ kW/cm^2). Thus, EGFP is much less prone to saturation effects than mNG and AcGFP. In summary, all three FPs perform well for the experimentally relevant excitation power densities up to 2 kW/cm^2, at which, for typical diffraction-limited detection volumes, mNG reaches a molecular brightness of ∼10 kHz/particle.

DISCUSSION

The spectroscopic analysis presented in this work aims to characterize fluorescence properties of recombinant mNG in comparison to *Aequorea* GFPs. The superior brightness reported for mNG based on bulk fluorescence (11) is confirmed at the single-molecule level. The linear range of fluorescence emission as a function of the excitation power density is reduced for mNG as compared to EGFP but still sufficiently broad to employ the typical excitation powers of confocal imaging and FCS applications. Within this power range, CPP up to 10 kHz/particle can be achieved for mNG in confocal FCS without compromising linearity. The diffusion of all three FP variants suggests a monomeric state in solution; none showed aggregation behavior either in bulk cuvette experiments or in FCS measurements. As such, mNG outperforms *Aequorea* GFPs for biochemical analysis when excited with the classical argon laser lines (488 or 514 nm).

However, pH-dependent sets of mNG absorption spectra indicate a more complex photophysical signature of this FP. In contrast to EGFP, for which a single protonation step converts the fluorescent anionic form into a nonfluorescent neutral form, mNG fluorescence is quenched by protonation under acidic conditions and, additionally, by deprotonation at very high pH. In the neutral-to-basic regime, two electronic forms of mNG coexist, whereas in the acidic regime, because of external protonation, the number of coexisting forms increases to three. Importantly, when using 488-nm excitation, two independent observations suggest that the neutral and basic forms of mNG have almost the same molecular brightness. First, the total fluorescence can be fairly well-reconstructed by the relative contributions of the basic and neutral forms. Second, when correctly accounting for flickering in FCS, CPP values show a similar pH dependence as bulk fluorescence. The latter indicates that the fitted amplitudes in FCS analysis reflect true particle numbers, which in turn implies that the two forms have very close fluorescence quantum yields. As a result, the neutral and basic forms appear indistinguishable in intensity-based applications; the number of counts in pixels of confocal images, as well as the particle numbers in FCS, represent a faithful readout for the concentration of mNG protein in the observed sample volume.

Blind spectral unmixing of absorption spectra

Disentangling the interconversion of two states in sets of absorption spectra, all crossing in the same isosbestic points, is relatively easy and can be carried out in different ways, including the approach based on NNMF. Blind spectral unmixing by NNMF gains its full power, however, in cases in which more than two states coexist simultaneously and interconvert into each other as a function of a control parameter. In terms of absorption spectra, such a system does not exhibit a common set of isosbestic points over the entire range of the control parameter, which is exactly the situation we observed for mNG, for which two distinct isosbestic points were identified in the extreme acidic and basic regimes (Fig. 1). Here, by using this approach, we were able not only to reconstruct the elementary spectra that represent electronic substates of the mNG chromophore but also obtained their relative contributions as a function of pH, a quantity that can be compared with independent experimental readouts. Thus, the approach provides an exciting framework to consistently link spectroscopically defined electronic substates with bulk fluorescence behavior as well as photodynamic properties resolved at the single-molecule level.

The core assumption of the NNMF approach is that the system exhibits a finite number of states, each of them characterized by a particular absorption spectrum, whose shape and position do not depend on the control parameter. In reality, these assumptions are not always met. Indeed, as is observed for both EGFP and mNG, at extreme pH conditions, conformational changes of the barrel structure globally affect the chromophore and, hence, its spectral features. For example, below pH 3.8, successive protonation of mNG not only further populates the protonated state of the chromophore (A-band) but also induces a gradual blue shift of the absorption band. Thus, those spectra cannot be included in the NNMF-based analysis, and the range of control parameters should be appropriately restricted. Furthermore, in reality, at the limits of this restricted range, still more than one form may contribute to the observed absorption spectrum. Based on the data alone, however, the algorithm cannot make a distinction between mixtures of several states or single states with complex absorption bands. As a result, the algorithm tends to treat the limiting spectrum as an elementary shape, which may lead to the appearance of ghost bands in reconstructed elementary spectra. Our analysis suggests that ghost bands tend to vanish when systematically extending the control parameter range (in our case, pH). We believe that such trends can successfully be used for their identification and elimination. To judge on the chemical identity of one or several states associated with elementary forms as revealed by the NNMF

analysis, one would have to bring in additional experimental and mathematical approaches.

A conceptually similar data analysis approach was recently used to study absorption spectra of pH-sensitive avGFP mutants (29). For some mutants, the reconstructed spectra of the acidic form showed simultaneously both A- and B-band contributions, which were termed "mixed states" and explained by a two-site protonation model (29). In light of this discussion, it seems very likely that the presence of the B-band in these cases was a spectrum reconstruction artifact.

FCS

In the FCS data of avGFPs, the concomitant rise of both the magnitude of A-band absorption as well as the flicker fractions and rates in the acidic regime provides compelling evidence for observing well-defined transitions between an anionic fluorescent state and a protonated nonfluorescent state of the chromophore (37,40,42,43). This could be confirmed for mNG, for which external protonation leads to a consistent rise of flickering upon acidification. In contrast to avGFPs, however, the mNG flicker rates are one order of magnitude smaller and, surprisingly, pH independent. The fact that protonation is not diffusion-controlled suggests slow conformational rearrangements of the tertiary structure as a prerequisite for protonation of the chromophore.

In the neutral-to-basic regime, interpretation of the flicker processes appears to be more complicated even when revisiting avGFPs. Haupts et al. claimed that the plateau behavior of residual flickering is a result of "internal" protonation (37). However, this model bears the implicit assumption that the proton wires leading to external protonation of the phenolic hydroxy group (Y66) and those leading to internal protonation are topologically disconnected. Otherwise, it is not clear why "internal" protons transiently quenching the chromophore at the same phenolic hydroxy group would not be exchanged with bulk solution. Elsliger et al. pointed out that proton acceptor sites different from the phenolic hydroxy group are unlikely to exist within the accessible pH range (30). Based on excitation power dependences in FCS data, other groups have claimed that photoinduced isomerization represents a more likely cause for flickering in the neutral-to-basic regime (39,51). Our FCS data also point toward this direction, because we observe a pronounced excitation power dependence of the flicker rates and amplitudes for all three FP variants at previously unexplored low excitation power densities.

In this context, it is striking that we observe for mNG at both extremes of the pH spectrum protonation events with opposite effects. Although under acidic conditions protonation amplifies flickering, under basic conditions it is deprotonation, a finding that cannot be reconciled within the framework of internal protonation. The pH-dependence of the slow flicker fraction associated with external protonation is closely correlated with the buildup of the contributions of the nonfluorescent acidic form as determined by blind spectral unmixing. In contrast, the pH-dependent contributions of the neutral and basic forms determined by blind spectral unmixing and the fluorescence flicker fractions measured at different pH by FCS do not superimpose. Thus, it is unlikely that flickering represents transitions between these two forms. This notion is corroborated by reconstructing the total fluorescence intensity, which suggests that the basic and neutral forms have similar molecular brightness and appear therefore indistinguishable in FCS. The remarkably constant pH-independent fraction of fast flickering in the regime in which the basic and neutral forms interconvert suggests rather that populating the dark states is governed by a generic mechanism with equal transition rates for both forms. In the basic regime, the pK_a values marking the decrease of the total fluorescence, the decrease of the CPP, and the rise of flicker fractions consistently match at about pH 10, suggesting a critical conformational change in the chromophore environment that reinforces the population of dark states. In this line of thinking, the removal of a second proton could have an indirect effect of reducing the number of H-bonds in the immediate chromophore environment, thus leading to more structural flexibility and subsequently a higher probability for internal conversion (35). Furthermore, the transition at pH 10 coincides with a kink leading to a sudden rise in the contributions of the basic form. Thus, the same protonation/deprotonation event at around pH 10 may represent the underlying cause for both behaviors—flickering as well as the build-up of the basic form—albeit without suggesting a causal relationship between them.

Structural considerations

The behavior of pH-dependent fluorescence emission is influenced by the topology of the H-bonding network that stably positions the chromophore within the FP barrel. The pattern of H-bonds connecting the phenolic hydroxy group (Y66 in wild-type avGFP, Y67 in EGFP, and Y69 in mNG) of the chromophore in EGFP and mNG with nearest neighbors is quite similar (Fig. 6 A); three H-bond donors are located within a distance of 3.3 Å or less. Two of them engage either two water molecules, as in the case of mNG, or a water and a hydroxy group of the threonine side chain (T204), as in the case of EGFP. One additional H-bond links the chromophore with an amino acid side chain for which the pK_a is of comparable magnitude as the chromophore itself (phenolic hydroxy group in avGFPs: pK_a = 8.0–8.2 (56), histidine (EGFP) pK_a ∼6.0, and cysteine (mNG) pK_a ∼8.2). In conclusion, the arrangement of H-bond donors in mNG and EGFP is very similar considering the pK_a values of the participants and their distances. In avGFPs, H148 was identified as a proton barrier, and the
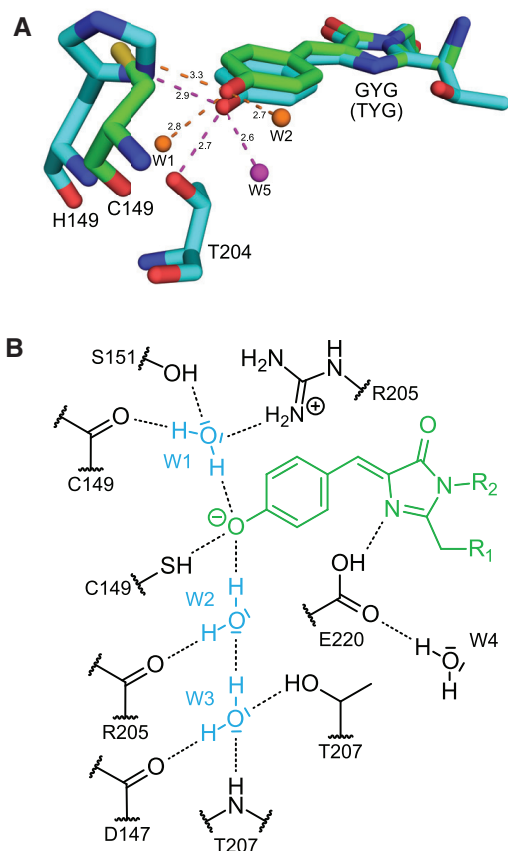
FIGURE 6 Chromophore environment of mNG (PDB: 5LTR) and EGFP (PDB: 2Y0G) at pH 8.0. (*A*) An overlaying stick representation of the chromophores of mNG (*green*) and EGFP (*cyan*) and the associated H-bond donors to the Y69 or Y67 hydroxy group is given. H-bonds are shown as dashed lines (*orange* for mNG or *magenta* for EGFP), with distances in Ångströms. (*B*) A proposed H-bond network in close vicinity to the mNG chromophore (*green*) is shown. Anionic state of the chromophore is stabilized by structural water (W1–4 corresponding to W430, W423, W503, and W413, respectively) and H-bonding of E220 with the imidazolinone moiety (N2).

mutation H148G shifted the pK_a of the protein to a level that was measured for isolated chromophores (24). Later, this role was confirmed by FCS analysis, in which the mutation H148G led to threefold increased flicker rates associated with external protonation (39). However, the slow pH-independent flickering of mNG in acidic buffers contradicts a corresponding role for C149.

A closer inspection of the chromophore environment of mNG (34) revealed some structural features that may explain its unusual spectroscopic behavior (Fig. 6 *B*). In contrast to E222 in avGFPs, the carboxyl group of glutamate E220 in mNG is positioned at an H-bonding distance to the imidazolinone moiety (N2) of the chromophore and is most likely protonated (distances 2.7 Å in mNG and 3.8 Å in EGFP). This configuration suggests stabilizing of the chromophore in the anionic state (B-band absorption) and appears incompatible with the role of a proton acceptor for ESPT. The H-bonding network of E220 in mNG seems to

be entirely disconnected from the hydroxy group of Y69. Similar configurations were described for structurally closely related copepode FPs (57), as well as for a second generation of the dsRed-derived "fruits" (58). Instead, the charged arginine (R205) could provide a relay function for the protonation of Y69, which is associated with external protonation and flickering. A reduced distance of the positively charged guanidinium ion (R205) in the basic form of mNG, as compared to the neutral form, could also explain the gradual hypsochromic shift observed in absorption spectra at increasing pH.

In contrast to EGFP, in which one water molecule is located close to Y67, the mNG chromophore is surrounded by three structural water molecules. In avGFPs, large stretches of unstructured protein backbone connected to strand 7 were proposed to promote water exchange in this area (26). In mNG, these parts are far more structured and compact, suggesting that water exchange is impaired (Fig. S8 *A*). Moreover, analyzing the topology of potential hydrogen donors and acceptors of these three water molecules implies considerable constraints for their orientation. We noticed that the proton wiring paths seem to be spatially confined by the side chains S151, R205, and T207, as well as by carbonyls and secondary amines of the protein backbone (Fig. 6 *B*), such that transfer routes toward bulk solution are hard to envision. The cavity appears closed in contrast to several exit routes that have been worked out for avGFPs (58–60). Thus, the slow protonation rates, their pH-independence, and the overall moderate flicker fraction found for mNG may reflect slow, major rearrangements of the β-barrel involving the strands 7, 8, and 10 (Fig. S8 *B*).

To date, FP variants used in the green color range are based almost exclusively on avGFPs from the cnidaria phylum. Their widespread application, accompanied by ongoing engineering efforts to optimize fluorescence properties, led to a large variety of mutants optimized for a broad variety of experimental needs (1). However, the close structural relation of β-barrels of hydrozoan FPs may impose restrictions for finding superior avGFP variants. From an evolutionary perspective, hydrozoan FPs represent only a small branch of the GFP family (61). In particular, some selected bilaterian GFPs exhibit extraordinary high extinction coefficients and fluorescence quantum yields (62–64) and, thus, represent excellent options and interesting targets for further research.

SUPPORTING MATERIAL

AUTHOR CONTRIBUTIONS

F.S. performed the experiments, analyzed the data, and provided all figures. E.P.P. analyzed steady-state spectroscopy data and contributed to FCS data

REFERENCES

1. Dedecker, P., F. C. De Schryver, and J. Hofkens. 2013. Fluorescent proteins: shine on, you crazy diamond. *J. Am. Chem. Soc.* 135:2387–2402.

2. Remington, S. J. 2011. Green fluorescent protein: a perspective. *Protein Sci.* 20:1509–1519.

3. Tsien, R. Y. 1998. The green fluorescent protein. *Annu. Rev. Biochem.* 67:509–544.

4. Toomre, D., and J. Bewersdorf. 2010. A new wave of cellular imaging. *Annu. Rev. Cell Dev. Biol.* 26:285–314.

5. Weidemann, T., J. Mücksch, and P. Schwille. 2014. Fluorescence fluctuation microscopy: a diversified arsenal of methods to investigate molecular dynamics inside cells. *Curr. Opin. Struct. Biol.* 28:69–76.

6. Chudakov, D. M., M. V. Matz, …, K. A. Lukyanov. 2010. Fluorescent proteins and their applications in imaging living cells and tissues. *Physiol. Rev.* 90:1103–1163.

7. Nienhaus, K., and G. U. Nienhaus. 2014. Fluorescent proteins for live-cell imaging with super-resolution. *Chem. Soc. Rev.* 43:1088–1106.

8. Shaner, N. C., G. H. Patterson, and M. W. Davidson. 2007. Advances in fluorescent protein technology. *J. Cell Sci.* 120:4247–4260.

9. Campbell, R. E., O. Tour, …, R. Y. Tsien. 2002. A monomeric red fluorescent protein. *Proc. Natl. Acad. Sci. USA.* 99:7877–7882.

10. Shaner, N. C., M. Z. Lin, …, R. Y. Tsien. 2008. Improving the photostability of bright monomeric orange and red fluorescent proteins. *Nat. Methods.* 5:545–551.

11. Shaner, N. C., G. G. Lambert, …, J. Wang. 2013. A bright monomeric green fluorescent protein derived from Branchiostoma lanceolatum. *Nat. Methods.* 10:407–409.

12. Pletnev, V. Z., N. V. Pletneva, …, S. Pletnev. 2013. Structure of the red fluorescent protein from a lancelet (Branchiostoma lanceolatum): a novel GYG chromophore covalently bound to a nearby tyrosine. *Acta Crystallogr. D Biol. Crystallogr.* 69:1850–1860.

13. Heppert, J. K., D. J. Dickinson, …, B. Goldstein. 2016. Comparative assessment of fluorescent proteins for in vivo imaging in an animal model system. *Mol. Biol. Cell.* 27:3385–3394.

14. Hostettler, L., L. Grundy, …, D. A. Glauser. 2017. The bright fluorescent protein mNeonGreen facilitates protein expression analysis in vivo. *G3 (Bethesda).* 7:607–615.

15. Barykina, N. V., O. M. Subach, …, G. N. Enikolopov. 2016. A new design for a green calcium indicator with a smaller size and a reduced number of calcium-binding sites. *Sci. Rep.* 6:34447.

16. Ormö, M., A. B. Cubitt, …, S. J. Remington. 1996. Crystal structure of the Aequorea victoria green fluorescent protein. *Science.* 273:1392–1395.

17. Ward, W. W., H. J. Prentice, …, S. C. Reeves. 1982. Spectral perturbations of the Aequorea green-fluorescent protein. *Photochem. Photobiol.* 35:803–808.

18. Bokman, S. H., and W. W. Ward. 1981. Renaturation of Aequorea green-fluorescent protein. *Biochem. Biophys. Res. Commun.* 101:1372–1380.

19. Chattoraj, M., B. A. King, …, S. G. Boxer. 1996. Ultra-fast excited state dynamics in green fluorescent protein: multiple states and proton transfer. *Proc. Natl. Acad. Sci. USA.* 93:8362–8367.

20. Lossau, H., A. Kummer, …, M. E. Michel-Beyerle. 1996. Time-resolved spectroscopy of wild-type and mutant green fluorescent proteins reveals excited state deprotonation consistent with fluorophore-protein interactions. *Chem. Phys.* 213:1–16.

21. Brejc, K., T. K. Sixma, …, S. J. Remington. 1997. Structural basis for dual excitation and photoisomerization of the Aequorea victoria green fluorescent protein. *Proc. Natl. Acad. Sci. USA.* 94:2306–2311.

22. Palm, G. J., A. Zdanov, …, A. Wlodawer. 1997. The structural basis for spectral variations in green fluorescent protein. *Nat. Struct. Biol.* 4:361–365.

23. Wiehler, J., G. Jung, …, B. Steipe. 2003. Mutagenic stabilization of the photocycle intermediate of green fluorescent protein (GFP). *ChemBioChem.* 4:1164–1171.

24. Wachter, R. M., M. A. Elsliger, …, S. J. Remington. 1998. Structural basis of spectral shifts in the yellow-emission variants of green fluorescent protein. *Structure.* 6:1267–1277.

25. Seifert, M. H., J. Georgescu, …, T. A. Holak. 2003. Backbone dynamics of green fluorescent protein and the effect of histidine 148 substitution. *Biochemistry.* 42:2500–2512.

26. Shinobu, A., and N. Agmon. 2015. The hole in the barrel: water exchange at the GFP chromophore. *J. Phys. Chem. B.* 119:3464–3478.

27. Shinobu, A., and N. Agmon. 2017. Proton wire dynamics in the green fluorescent protein. *J. Chem. Theory Comput.* 13:353–369.

28. Abbruzzetti, S., E. Grandi, …, A. Mozzarelli. 2005. Kinetics of acid-induced spectral changes in the GFPmut2 chromophore. *J. Am. Chem. Soc.* 127:626–635.

29. Bizzarri, R., R. Nifosì, …, F. Beltram. 2007. Green fluorescent protein ground states: the influence of a second protonation site near the chromophore. *Biochemistry.* 46:5494–5504.

30. Elsliger, M. A., R. M. Wachter, …, S. J. Remington. 1999. Structural and spectral response of green fluorescent protein variants to changes in pH. *Biochemistry.* 38:5296–5301.

31. Hanson, G. T., T. B. McAnaney, …, S. J. Remington. 2002. Green fluorescent protein variants as ratiometric dual emission pH sensors. 1. Structural characterization and preliminary application. *Biochemistry.* 41:15477–15488.

32. Nienhaus, K., F. Renzi, …, G. U. Nienhaus. 2006. Exploring chromophore–protein interactions in fluorescent protein cmFP512 from Cerianthus membranaceus: X-ray structure analysis and optical spectroscopy. *Biochemistry.* 45:12942–12953.

33. Oltrogge, L. M., Q. Wang, and S. G. Boxer. 2014. Ground-state proton transfer kinetics in green fluorescent protein. *Biochemistry.* 53:5947–5957.

34. Clavel, D., G. Gotthard, …, A. Royant. 2016. Structural analysis of the bright monomeric yellow-green fluorescent protein mNeonGreen obtained by directed evolution. *Acta Crystallogr. D Struct. Biol.* 72:1298–1307.

35. Jung, G., J. Wiehler, and A. Zumbusch. 2005. The photophysics of green fluorescent protein: influence of the key amino acids at positions 65, 203, and 222. *Biophys. J.* 88:1932–1947.

36. Dickson, R. M., A. B. Cubitt, …, W. E. Moerner. 1997. On/off blinking and switching behaviour of single molecules of green fluorescent protein. *Nature.* 388:355–358.

37. Haupts, U., S. Maiti, …, W. W. Webb. 1998. Dynamics of fluorescence fluctuations in green fluorescent protein observed by fluorescence correlation spectroscopy. *Proc. Natl. Acad. Sci. USA.* 95:13573–13578.

38. Petrov, E. P., and P. Schwille. 2008. State of the art and novel trends in fluorescence correlation spectroscopy. *In* Standardization and Quality Assurance in Fluorescence Measurements II: Bioanalytical and Biomedical Applications. U. Resch-Genger, ed. Springer, pp. 145–197.

39. Bosisio, C., V. Quercioli, …, G. Chirico. 2008. Protonation and conformational dynamics of GFP mutants by two-photon excitation fluorescence correlation spectroscopy. *J. Phys. Chem. B.* 112:8806–8814.

40. Heikal, A. A., S. T. Hess, …, W. W. Webb. 2000. Molecular spectroscopy and dynamics of intrinsically fluorescent proteins: coral red (dsRed) and yellow (Citrine). *Proc. Natl. Acad. Sci. USA*. 97:11996–12001.

41. Liu, Y., H. R. Kim, and A. A. Heikal. 2006. Structural basis of fluorescence fluctuation dynamics of green fluorescent proteins in acidic environments. *J. Phys. Chem. B*. 110:24138–24146.

42. Schwille, P., S. Kummer, …, W. W. Webb. 2000. Fluorescence correlation spectroscopy reveals fast optical excitation-driven intramolecular dynamics of yellow fluorescent proteins. *Proc. Natl. Acad. Sci. USA*. 97:151–156.

43. Widengren, J., B. Terry, and R. Rigler. 1999. Protonation kinetics of GFP and FITC investigated by FCS - aspects of the use of fluorescent indicators for measuring pH. *Chem. Phys*. 249:259–271.

44. Hansen, P. C. 1998. Rank-Deficient and Discrete Ill-Posed Problems: Numerical Aspects of Linear Inversion. Society for Industrial and Applied Mathematics, Philadelphia, PA.

45. Berry, M. W., M. Browne, …, R. J. Plemmons. 2007. Algorithms and applications for approximate nonnegative matrix factorization. *Comput. Stat. Data Anal*. 52:155–173.

46. Lee, D. D., and H. S. Seung. 1999. Learning the parts of objects by nonnegative matrix factorization. *Nature*. 401:788–791.

47. Paatero, P., and U. Tapper. 1994. Positive matrix factorization: a nonnegative factor model with optimal utilization of error estimates of data values. *Environmetrics*. 5:111–126.

48. Lawson, C. L., and R. J. Hanson. 1974. Solving Least Squares Problems. Prentice Hall, Englewood Cliffs, NJ.

49. Widengren, J., Ü. Mets, and R. Rigler. 1995. Fluorescence correlation spectroscopy of triplet states in solution: a theoretical and experimental study. *J. Phys. Chem*. 99:13368–13379.

50. Petrov, E. P., T. Ohrt, …, P. Schwille. 2006. Diffusion and segmental dynamics of double-stranded DNA. *Phys. Rev. Lett*. 97:258101.

51. Widengren, J., U. Mets, and R. Rigler. 1999. Photodynamic properties of green fluorescent proteins investigated by fluorescence correlation spectroscopy. *Chem. Phys*. 250:171–186.

52. Müller, P., P. Schwille, and T. Weidemann. 2014. PyCorrFit-generic data evaluation for fluorescence correlation spectroscopy. *Bioinformatics*. 30:2532–2533.

53. Ward, W. W., and S. H. Bokman. 1982. Reversible denaturation of Aequorea green-fluorescent protein: physical separation and characterization of the renatured protein. *Biochemistry*. 21:4535–4540.

54. Petrásek, Z., and P. Schwille. 2008. Precise measurement of diffusion coefficients using scanning fluorescence correlation spectroscopy. *Biophys. J*. 94:1437–1448.

55. Eggeling, C., J. Widengren, …, C. A. Seidel. 1998. Photobleaching of fluorescent dyes under conditions used for single-molecule detection: evidence of two-step photolysis. *Anal. Chem*. 70:2651–2659.

56. Bell, A. F., X. He, …, P. J. Tonge. 2000. Probing the ground state structure of the green fluorescent protein chromophore using Raman spectroscopy. *Biochemistry*. 39:4423–4431.

57. Wilmann, P. G., J. Battad, …, J. Rossjohn. 2006. The 2.1A crystal structure of copGFP, a representative member of the copepod clade within the green fluorescent protein superfamily. *J. Mol. Biol*. 359:890–900.

58. Shu, X., N. C. Shaner, …, S. J. Remington. 2006. Novel chromophores and buried charges control color in mFruits. *Biochemistry*. 45:9639–9647.

59. Agmon, N. 2005. Proton pathways in green fluorescent protein. *Biophys. J*. 88:2452–2461.

60. Shinobu, A., G. J. Palm, …, N. Agmon. 2010. Visualizing proton antenna in a high-resolution green fluorescent protein structure. *J. Am. Chem. Soc*. 132:11093–11102.

61. Shagin, D. A., E. V. Barsova, …, M. V. Matz. 2004. GFP-like proteins as ubiquitous metazoan superfamily: evolution of functional features and structural complexity. *Mol. Biol. Evol*. 21:841–850.

62. Bomati, E. K., J. E. Haley, …, D. D. Deheyn. 2014. Spectral and structural comparison between bright and dim green fluorescent proteins in Amphioxus. *Sci. Rep*. 4:5469.

63. Evdokimov, A. G., M. E. Pokross, …, D. M. Chudakov. 2006. Structural basis for the fast maturation of Arthropoda green fluorescent protein. *EMBO Rep*. 7:1006–1012.

64. Tanida-Miyake, E., M. Koike, …, I. Tanida. 2018. Optimization of mNeonGreen for Homo sapiens increases its fluorescent intensity in mammalian cells. *PLoS One*. 13:e0191108.